**3964** *J. Phys. Chem. A* **2000,** *104,* 3964−3973

# Temperature Dependent Kinetics of the OH/HO$_2$/O$_3$ Chain Reaction by Time-Resolved IR Laser Absorption Spectroscopy

**Sergey A. Nizkorodov, Warren W. Harper, Bradley W. Blackmon, and David J. Nesbitt***

*JILA, National Institute of Standards and Technology and University of Colorado, and Department of Chemistry and Biochemistry, University of Colorado, Boulder, Colorado 80309-0440*

*Received: September 30, 1999; In Final Form: January 11, 2000*

This paper presents an extensive temperature dependent kinetic study of the catalytic HO$_x$ ozone cycle, (1) OH + O$_3$ → HO$_2$ + O$_2$ and (2) HO$_2$ + O$_3$ → OH + 2 O$_2$, based on time-resolved, Doppler limited direct absorption spectroscopy of OH with a single mode ($\Delta\nu = 0.0001$ cm$^{-1}$) high-resolution infrared laser. The sum of the two chain rate constants, $k_1 + k_2$, is measured over the 190−315 K temperature range and can be accurately described by an Arrhenius-type expression: $k_1 + k_2$ (cm$^3$/s) = 2.26(40) × 10$^{-12}$ exp[−976(50)/*T*]. These results are in excellent agreement with studies by Ravishankara et al. [*J. Chem. Phys.* **1979**, *70*, 984] and Smith et al. [*Int. J. Chem. Kinet.* **1984**, *16*, 41] but are significantly higher than the values currently accepted for atmospheric modeling. In addition, these studies also reflect the first such rate measurements to access the 190−230 K temperature range relevant to kinetic modeling of ozone chain loss in the lower stratosphere.

## I. Introduction

The so-called catalytic odd hydrogen (HO$_x$) ozone cycle,[1,2]

$$OH + O_3 \rightarrow HO_2 + O_2 \quad (1)$$

$$HO_2 + O_3 \rightarrow OH + 2\,O_2 \quad (2)$$

is one of the most important atmospheric processes leading to the natural destruction of atmospheric ozone. This cycle is particularly active at lower stratospheric altitudes (20−30 km, 190−230 K) in the mid-latitudes. Indeed, the HO$_x$ chain reaction is estimated to be responsible for nearly *half* of the global ozone loss in the stratosphere.[3] This makes it especially important to have accurate knowledge of the temperature dependent rate constants $k_1$ and $k_2$ for reliable modeling of atmospheric ozone phenomena.

Reactions 1 and 2 have been studied by a number of research groups. The first direct experimental measurement of $k_1$ was performed in 1973 by Anderson and Kaufman,[4] who reported this rate constant between 220 and 450 K. These studies reacted H atoms with NO$_2$ to prepare OH radicals in a conventional flow-tube apparatus, with the HO$_x$ chain reaction monitored as a function of time (i.e., the distance for a well-characterized flow velocity) via resonance OH fluorescence on the $A^2\Sigma \leftarrow X^2\Pi$ band. Shortly thereafter, Kurylo[5] performed room temperature studies of $k_1$ using pulsed UV laser photolysis of O$_3$ followed by the fast reaction of O($^1$D) photofragments with H$_2$ to generate OH, which again was detected via resonant fluorescence. In a later study by Ravishankara et al.,[6] $k_1$ was measured via similar flash photolysis/resonance fluorescence methods over a temperature range of 238−357 K. Of particular relevance to the present work, however, these authors were first to point out the profound complications caused by vibrationally excited OH on the observed kinetics (see below). The results reported by Ravishankara et al. indicate $k_1$ to be systematically higher (by up to 40%) compared with the earlier data of refs 4 and 5. Subsequent measurements of $k_1$ have also been obtained via laser induced fluorescence by Smith and co-workers ($T$ = 240−295 K)[7] and laser magnetic resonance methods by Zahniser and Howard (298 K),[8] with results in substantially good agreement with the higher values of Ravishankara et al.[6]

It is important to note at the outset that although these previous studies nominally obtain values of $k_1$ by analysis of OH removal as a single exponential process, this is not strictly correct for a two center chemical chain reaction. Indeed, as described in a previous kinetic analysis,[9] the loss of OH is rigorously given by (i) a single exponential *induction* decay characterized by the *sum* of the two chain rates ($k_1 + k_2$) followed by (ii) a steady-state *propagation* regime where OH is maintained at a constant level $\approx k_2/(k_1 + k_2)[OH]_0$ by chain reactions 1 and 2. However, since this induction rate is typically dominated by the first step (i.e., $k_1 >> k_2$), direct observation of these finite, steady-state OH levels in the propagation regime requires especially high signal to noise methods. Such methods have been recently demonstrated in our laboratory, based on shot noise limited direct absorption of a single mode laser to detect the OH radicals.[9] Exponential analysis of the fast chain induction kinetics yields a room temperature rate sum of $k_1 + k_2 = 8.4(8) \times 10^{-14}$ (cm$^3$/molecule)/s, which is in excellent agreement with the 300 K data of Ravishankara et al.[6]

Measurements of the HO$_2$ + O$_3$ reaction rate constant have proven more challenging since $k_2$ is at least an order of magnitude smaller than $k_1$ under usual stratospheric and laboratory temperatures (200 K ≤ $T$ ≤ 400 K), and thus any OH formed in reaction 2 quickly regenerates HO$_2$ via reaction 1. One approach to decouple the effects of reaction 1 is to use an efficient scavenger which reacts quickly with OH but is inert to HO$_2$. This method has been successfully demonstrated by Zahniser and Howard,[8] Manzanares et al.,[10] and Wang et al.,[11] who used either C$_3$H$_8$ or C$_2$F$_3$Cl for chemical removal of OH. One very clever method by Sinha et al.[12] exploits isotopically labeled H$^{18}$O$_2$ in excess $^{16}$O$_3$ reagent with laser magnetic

10.1021/jp9934984 CCC: $19.00

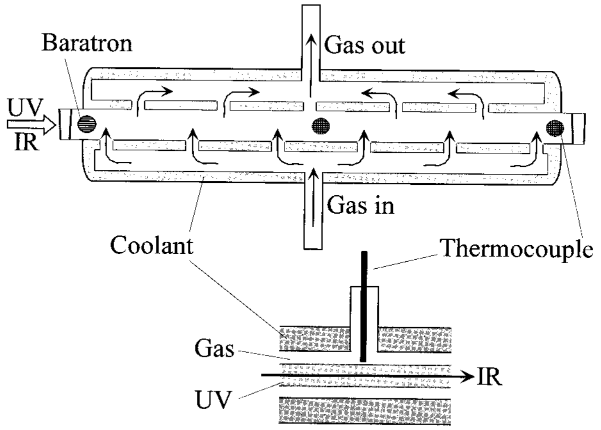

**Figure 1.** Schematic cut through the temperature-controlled flow cell (top view). The gas inlet and outlet manifolds are designed such that the gas flows *across* the cell through multiple entry and exit points, which serves to reduce temperature and concentration gradients along the length of the cell. Surrounding the reaction chamber is a cooling jacket through which a temperature-controlled fluid is pumped. Circles indicate the placements of a baratron and two thermocouple gauges for in situ measurements of the gas pressure and temperature. The bottom drawing shows how the thermocouples are positioned (side view).

resonance detection of the $H^{18}O_2$. Via this detection scheme, neither the $^{18}OH$ nor $^{16}OH$ product of reaction 1 is able to regenerate $H^{18}O_2$ via reaction with $^{16}O_3$, thus isotopically breaking the chain cycle. The combination of these measurements has yielded results over a 233−450 K range, but which show upward curvature in the Arrhenius plot at the lowest temperatures. Results obtained by different groups are in fairly good agreement particularly at room temperature and below.[11]

In spite of this wealth of experimental studies,[4−12] the values of $k_1$ and $k_2$ in the temperature range relevant to the lower stratosphere (190−230 K) are still partly based on extrapolations. For example, the value of $k_1$ used currently in stratospheric modeling[13] represents an average of results obtained in refs 4−8. Ravishankara et al.[6] determined $k_1$ in the 238−357 K temperature window, but their attempts to reach lower temperatures were precluded by strong kinetic interference from vibrationally excited OH radicals. Though the lowest temperatures (223 K) studied by Anderson and Kaufman[4] sample the top of this stratospheric window, their results at higher temperatures are unfortunately not in good agreement with the data of Ravishankara et al.[6] Similarly, $k_2$ has been determined down to 233 K, but extrapolation to lower temperatures is even more problematic due to strong curvature in the Arrhenius plots[11,12] mentioned above. In summary, there is a need for extension of the available experimental data on OH/$HO_2$/$O_3$ chemical chain reactions down to temperatures characteristic of the lower stratosphere.

The lack of reliable low-temperature data has prompted us to use alternative methods based on high-resolution infrared (IR) direct absorption spectroscopy to study the kinetics of reactions 1 and 2.[9] There are several important advantages in direct absorption versus fluorescence detection of OH. (i) The method is quite general and equally applicable to detection of both $HO_2$ and OH radicals, which are the key players in the $HO_x$ ozone cycle. (ii) IR absorption line strengths are accurately known for both species;[14−19] thus, the measurements can easily be converted into *absolute* number densities of each radical species. (iii) IR radiation in this range is not absorbed by $O_3$ as opposed to the near-UV light at around 308 nm used to probe OH in the fluorescence-based methods. This permits the rate constant to be measured over a substantially extended range of $O_3$ densities compared to previous studies of the reaction. Under these conditions of increased $O_3$ density, the chain nature of the $HO_x$ cycle, which had proven difficult to detect unambiguously in previous kinetic studies of the reaction, becomes experimentally quite important.[9] (iv) IR detection allows the probing of a much broader range of rovibrational levels of OH, without interference from rapid predissociation effects in the upper $A^2\Sigma$ ($v \geq 2$ and/or high $N$) states of OH. (v) Most importantly, this broad tuning capability permits direct monitoring of vibrationally excited OH($v$,$N$) populations, and thus quantitative characterization of these important rovibrational relaxation processes. In our previous publication[9] (hereafter noted as paper I), direct IR absorption methods have been successfully applied to the measurement of $k_1 + k_2$ at 298 K. The main thrust of this paper is to extend these measurements to the lower temperature domain relevant to atmospheric modeling of the stratosphere. A recipe for separating this result into individual components ($k_1$ and $k_2$) is provided at the end of the paper, and the next efforts in this laboratory will concentrate on this challenging task.

The method and apparatus are essentially the same as those used previously, with suitable modifications to the flow cell for achieving variable, low-temperature flow conditions. The reaction sequence is initiated by a short pulse of UV radiation from an excimer laser. This pulse photodissociates a small fraction of $O_3$ in the reaction flow chamber into $O(^1D)$, which rapidly abstracts hydrogen atoms from $H_2O$ (or $H_2$ for the low-temperature studies) to form OH. The nascent rovibrational-state distribution of OH generated during this reaction sequence is generally quite "hot", particularly when $H_2$ is used as the reactant.[20−23] However, under favorable conditions, equilibration by collisions with the buffer gas is rapid compared to the characteristic time scales for reactions 1 and 2. Thus, formation of OH can be regarded for all practical purposes as essentially instantaneous, leading to substantial simplifications in the kinetic analysis. The time dependent densities of OH (and $HO_2$) are monitored in real time via high-resolution direct absorption spectroscopy, which is capable of fully resolving each vibrational, rotational, spin−orbit, and lambda-doublet state. The rate constants are then obtained from fitting the observed time dependence of OH densities to an appropriate kinetic model representation.

## II. Experimental Section

The experimental strategy is described in detail in paper I, and, except for a description of the modifications required for temperature dependent measurements, only a brief summary is given here.[9] The heart of the experimental apparatus is a newly designed temperature controlled flow cell shown in Figure 1. The reaction chamber is a tube, 106 cm long, 2.5 cm in diameter, with a volume of 0.52 L. The windows into the chamber are made of IR grade quartz optics, with a transmittance limited by surface reflection to >90% in both the near-IR ($\approx$3700 $cm^{-1}$) and UV ($\approx$308 nm). Each entrance to the reaction chamber has two such windows separated by an evacuated space, which serves to protect the inner optics from atmospheric water vapor condensation at reduced temperatures. The gas mixture enters and leaves the reaction chamber through the gas inlet/outlet manifold system that runs along the entire length of the tube (Figure 1). The net direction of the flow is *across* the reaction chamber as opposed to the previous design where the gas flows *along* the tube. The main advantage of such an arrangement is that fresh gas flows into each area of the chamber on a pulse by pulse basis, with the temperature and density gradients along the tube reduced to a minimum.

The gas inlet/outlet systems and the reaction chamber are surrounded by a cooling jacket, which contains a flowing fluid with a controlled temperature. For the present experiments, ethanol, *n*-pentane, and water are used as the cooling fluids, depending on the desired temperature range. The fluid is circulated by a 32 L/min pump between the cooling jacket of the flow cell and a copper heat-exchanger coil, immersed in a constant temperature bath. The temperature of the gas in the reaction chamber is measured by two K-type thermocouples in the center and at the edge of the cell (Figure 1). The thermocouples and the thermometer are periodically tested against temperature standards and found to be accurate to <1 K over the 180−350 K temperature range. For all of the experiments reported here, the two thermocouple readings in the cell are consistent both with each other and with the temperature of the circulating fluid to within $\Delta T \approx 1$ K (1.5 K for $T < 210$ K).

Ozone is produced from oxygen prior to the experiments with a commercial corona discharge ozone generator and trapped on silica gel beads at about 170 K. Ozone is delivered into the cell by passing a regulated flow of Ar through the trap warmed to 190−220 K. Apart from the $O_3$/Ar mixture, two other gases flow into the reaction chamber, one containing the OH precursor molecule ($H_2$ or $H_2O$) and the other a buffer gas. The partial flows and thus the partial pressures of the combined gases entering the reaction chamber are measured and controlled with a set of calibrated flow meters. The choice of the buffer gas and OH precursor molecule depends on the temperature range of interest. For $T > 245$ K, the OH precursor is formed by passing a known flow of Ar through a porous water bubbler, with Ar also as the buffer gas diluent. Under typical experimental conditions the cell can contain up to 3 Torr of $O_3$ and up to 5 Torr (1 Torr = 133.32 Pa) of $H_2O$ at a total pressure of 20−30 Torr, most of which is the Ar buffer. At lower temperatures, where the $H_2O$ vapor pressure becomes too low, Ar/$H_2O$ is replaced by $H_2$, while $CO_2$ is used as the buffer gas. $CO_2$ is chosen by virtue of its relatively efficient quenching of OH($v$,$N$) states (the quenching rate constants increase nearly exponentially with vibrational quantum number from $2 \times 10^{-13}$ cm$^3$/s (for $v = 1$) to $5 \times 10^{-11}$ cm$^3$/s (for $v = 9$)[24,25] and its chemical inertness to both OH and $HO_2$ chain radicals. For these lower temperature experiments, the flow cell normally contains 8−10 Torr $H_2$ and 9−14 Torr $CO_2$ in addition to the $O_3$/Ar mixture, again at a total pressure of 20−30 Torr. The total flow into the 0.52 L reaction chamber is normally of the order of 2−3 (Torr·L)/s, which means that the chamber is completely refreshed every 5 s (25−50 excimer laser pulses at the 5−10 Hz repetition rate of the experiment). With <2 (mJ/cm$^2$)/pulse of UV photolysis laser the chain reaction loss of ozone due to prior pulses in the flow cell is insignificant.

Because of the important role the absolute concentration of ozone plays in the determination of the rate constant, the $O_3$ density is always measured via *in situ* absorption of the XeCl excimer UV radiation used to dissociate $O_3$. This method has the advantage of excellent dynamic range and readily permits the determination of [$O_3$] in the range of $10^{15}$−$10^{17}$ cm$^{-3}$ through the 106 cm long flow cell. The UV absorbance can be converted into absolute density using $O^3$ absorption cross-sections[26−28] for $T = 195$−298 K. To account for small variations in the $O_3$ absorbance over the spectral output of the excimer laser, the ozone UV cross-section is taken as a weighted average of the two major XeCl emission lines at 307.9 and 308.2 nm.[29] Table 1 provides the resulting cross-sections for each relevant temperature point. Note that the cross-section values at *elevated* temperatures ($T > 298$ K) are based on extrapolations of data from ref 27 and are thus somewhat less accurate (10%) than the cross-sections at room temperature and below (4%). As a second independent test, the density of $O_3$ in the flow is additionally verified by absorption of a mercury UV lamp at 253.7 nm[30] before the gas is injected into the flow cell. The $O_3$ cell densities measured at these two wavelengths agree quantitatively after correcting for the temperature and pressure difference in the flow cell and Hg lamp cell (see paper I for more details).

**TABLE 1: Rate Constants Determined in This Study**[a]

| mixture | $T$ (K) | $O_3$ cross-section ($\times 10^{-19}$ cm$^2$) | $k_1 + k_2$ ($\times 10^{-14}$ cm$^3$/s) |
|---|---|---|---|
| a | 314.0 | 1.487 | 10.9 |
| a | 295.0 | 1.350 | 8.94 |
| a | 287.0 | 1.310 | 8.28 |
| b | 277.1 | 1.271 | 5.96 |
| a | 273.0 | 1.257 | 6.52 |
| b | 266.9 | 1.240 | 5.20 |
| a | 266.0 | 1.237 | 6.20 |
| b | 256.4 | 1.215 | 4.44 |
| a | 253.0 | 1.208 | 5.16 |
| b | 250.0 | 1.203 | 4.60 |
| b | 248.3 | 1.200 | 4.07 |
| b | 240.0 | 1.188 | 3.99 |
| b | 239.9 | 1.188 | 3.77 |
| b | 234.8 | 1.181 | 3.67 |
| b | 223.4 | 1.170 | 3.18 |
| b | 217.7 | 1.165 | 2.10 |
| b | 212.6 | 1.161 | 2.25 |
| b | 207.1 | 1.158 | 1.86 |
| b | 201.8 | 1.155 | 1.90 |
| b | 195.8 | 1.152 | 1.51 |
| b | 190.6 | 1.150 | 1.62 |

[a] The first and the second columns specify the flow cell mixture (a = Ar/$H_2O$/$O_3$; b = $CO_2$/$H_2$/$O_3$) and temperature for a given experimental run. The fourth column provides the resulting rate constant, $k_1 + k_2$, and the third column contains $O_3$ absorption cross-sections at 308 nm used to deduce the $O_3$ density from absorption measurements.[27] Estimated 95% confidence intervals amount to ±1 K for temperature (±1.5 K at $T < 210$ K), 15% for the rate constants, and ±4% for the $O_3$ UV cross-section (±10% for $T = 314$ K).

The temporal profile of the OH radical density is probed via absorption of a continuous single mode F-center laser (FCL)[31] tunable between 2.5 and 3.3 $\mu$m, with a line width of 2 MHz. The FCL radiation is split into several separate beams, one of which is directed through the flow cell to a signal InSb detector, another is focused onto a reference detector, and the rest is used for laser beam diagnostics. Both detectors are carefully impedance-matched and have ≈400 ns rise times. The centers of individual rovibrational transitions of OH are located to better than 0.002 cm$^{-1}$ accuracy using a home-built traveling Michelson interferometer (i.e., $\lambda$-meter) constructed after the design by Hall and Lee.[32] With the F-center laser centered on top of an OH absorption feature, the time dependent absorbance is measured as a transient imbalance between the signal and reference detector outputs. This difference is digitized by an oscilloscope and averaged for 500−2000 UV laser pulses. About 10−20% of 2500 sampled time points occur before the UV laser pulse to determine the zero level. The noise density in the resulting trace is (6−9) $\times 10^{-9}$ Hz$^{-1/2}$ at about 20 $\mu$W of IR laser power; this is equivalent to an absorption sensitivity of $<10^{-5}$ in the 1 MHz detection bandwidth. At room temperature for a Doppler broadened peak, this results in a detection sensitivity of $\leq 10^{10}$ cm$^{-3}$ for the total OH density (or $\leq 10^{9}$ cm$^{-3}$ per quantum state). Depending on the $O_3$ density, temperature, and UV laser power (nominally kept below 2 mJ/

$cm^2$/pulse to avoid secondary radical−radical processes), peak OH absorbances of $10^{-4}$ to $5 \times 10^{-3}$ are routinely observed, which translates into a peak signal-to-noise ratio of ≈10−500.

## III. Kinetic Analysis

A detailed kinetic treatment of the $HO_x$ chain reaction appropriate for the present experimental conditions has been described in paper I;[9] here we only provide a brief summary of this analysis along with necessary modifications for the low-temperature studies. The analysis is based on the following kinetic conditions being satisfied. (i) The processes leading to initial generation of OH are very rapid compared to the rates of reactions 1 and 2 and can be approximated by an instantaneous rise of OH density to $[OH]_0$ at $t = 0$. Furthermore, rovibrational relaxation with the buffer gas is sufficiently fast to maintain $OH(v,N)$ in a thermal distribution of quantum states. (ii) Total radical density is negligibly small compared to that of $O_3$ and other stable species, i.e., $[OH]_0 \ll [O_3]$, which allows treatment of reactions 1 and 2 as pseudo-first-order processes and neglect of radical−radical processes, at least on the fast time scales of the chain induction. (iii) On a much longer time scale, radicals OH and $HO_2$ undergo slower irreversible decay due to secondary reactions, diffusion from the laser probe region, and deactivation on the walls, which can be simply approximated by a first-order decay. Under these conditions, one can solve analytically for $[OH(t)]$ as a simple double exponential decay9

$$\frac{[OH](t)}{[OH]_0} = \frac{k_1}{k_1 + k_2}\, e^{-k_{ind}[O_3]t} + \frac{k_2}{k_1 + k_2}\, e^{-k_{term}t} \qquad (3)$$

where the chain induction rate constant is given by $k_{ind} = k_1 + k_2$ and the chain termination rate constant,

$$k_{term.} = \frac{k_{irr}^{OH} k_2}{k_1 + k_2} + \frac{k_{irr}^{HO_2} k_1}{k_1 + k_2} \qquad (4)$$

depends on the irreversible first order decay rates for OH and $HO_2$. The chain induction period is defined by $\tau_{ind} = (k_{ind}[O_3])^{-1}$, which is equal to the 1/*e* time of the induction process at a given $O_3$ density. Once again, since $k_1 \gg k_2$, the second term in eq 3 is normally much smaller than the dominant induction term; thus the double exponential decay behavior has been commonly ignored in previous kinetic analyses of the $OH + O_3$ reaction rates.

The validity and relative importance of these kinetic assumptions for the present study will be examined in more detail throughout the next sections. Here only the conditions necessary for a swift generation of thermally equilibrated OH are discussed. The primary chemical initiation step following the $O_3$ photolysis and resulting in generation of OH involves rapid reaction between $O(^1D)$ and a hydrogen containing species; e.g.,

$$O(^1D) + H_2O \rightarrow OH + OH \qquad (5)$$

$$O(^1D) + H_2 \rightarrow OH + H \qquad (6)$$

As explained in detail in paper I and in the study of Ravishankara et al.,[6] based on a similar chain initiation sequence, water is the optimal choice of OH precursor for several important reasons. (i) The degree of OH vibrational excitation[33] from reaction 5 is relatively modest ($v \leq 2$), which limits the extent of subsequent relaxation necessary to achieve thermalized kinetic conditions. (ii) In addition, $H_2O$ is an extremely efficient quencher for vibrationally excited OH (hereafter denoted simply as OH*).[34,35] This rapid vibrational relaxation is essential for reliable kinetic analysis and interpretation since OH* tends to react with $O_3$ much faster than the ground-state OH.[36,37] Reaction 5 is so fast ($k_5(298K) = 2.2 \times 10^{-10}$ $cm^3/s$)[11] that vibrational relaxation of the resulting OH represents by far the rate-limiting step for the experimental appearance of thermalized OH absorption and must occur in the shortest possible time. (iii) $H_2O$ is completely inert toward OH, with the exception of the rather high-barrier, irrelevant symmetric exchange reaction $H_2O + OH \leftrightarrow OH + H_2O$. Due to the combination of these favorable factors, OH can be produced and fully equilibrated under typical experimental conditions in less than 3−6 μs, which is 1−3 orders of magnitude smaller than the time scale of the chain induction period (100 μs to 20 ms). Thus, most kinetic measurements at $T > 245$K (including the room temperature study of paper I) have been performed with $H_2O/O_3/Ar$ flow using reaction 5 to prepare OH.

At sufficiently low cell temperatures, however, the $H_2O$ vapor pressure becomes vanishingly small, thus requiring other methods of OH generation. In this study we make use of reaction 6, which has a nearly gas kinetic rate constant of $k_6 = 1.0 \times 10^{-10}$ $cm^3/s$ at room temperature.[11] The disadvantage with this approach is that it results in an extremely “hot” nonequilibrium rovibrational distribution of OH. Specifically, reaction 6 produces OH with significant vibrational population[20−23] up to $v = 4$ and rotational excitation[38] up to $N > 25$, which can take considerable time to relax in the absence of an efficient OH* quencher such as $H_2O$.[32] To complicate matters further, the H atom product of reaction 6 undergoes fast secondary reaction with $O_3$ [$k_7(298K) = 2.9 \times 10^{-11}$ $cm^3/s$],[13]

$$H + O_3 \rightarrow OH(v \leq 9) + O_2 \qquad (7)$$

which is known from previous studies to generate a nascent OH product state distribution[39−41] peaking at $v \approx 7-9$, with some indications of a minor channel[42,43] for forming $OH(v=0-3)$ with extremely high rotational energies ($N \geq 33$). This highly excited OH rovibrational distribution necessarily requires extensive energy transfer with the flow cell gas mixture in order to reach thermal equilibrium. Thus, any time dependent kinetic probe of $HO_x$ chain kinetics monitored via $OH(v=1 \leftarrow 0)$ absorption can be contaminated by time dependent cascade relaxation processes, population in the upper state $OH(v=1)$, and premature formation of $HO_2$ by vibrationally accelerated reactions of $OH(v)$ with $O_3$.

As an explicit example of such behavior, Figure 2a demonstrates the temporal evolution of OH absorbance signals in an $Ar/H_2/O_3$ mixture monitored on specific $v = 3 \leftarrow 2$, $v = 2 \leftarrow 1$, and $v = 1 \leftarrow 0$ rovibrational transitions, which demonstrates several interesting effects. Most dramatically, *stimulated emission* is initially observed on the $v = 1 \leftarrow 0$ transition, which indicates the presence of a vibrational *population inversion* between $OH(v=0)$ and $OH(v=1)$ states at $t < 50$ μs. This emission strength initially grows with time, reflecting an increase in $OH(v=1)$ vs $OH(v=0)$ populations due to cascade relaxation from higher lying vibrational states. Eventually, however, this situation is reversed, and the absorbance signal becomes positive, eventually rising to a maximum level some 220 μs after the laser pulse and then slowly decaying due to competition between cascade relaxation and the $HO_x$ chain cycle. For the $v = 2 \leftarrow 1$ transition, no stimulated emission is observed and the signal reaches a maximum much sooner than for the $v = 1 \leftarrow 0$ transition, with subsequent decay due to reactive removal by $OH(v=1) + O_3$ and cascade relaxation. It is interesting to note

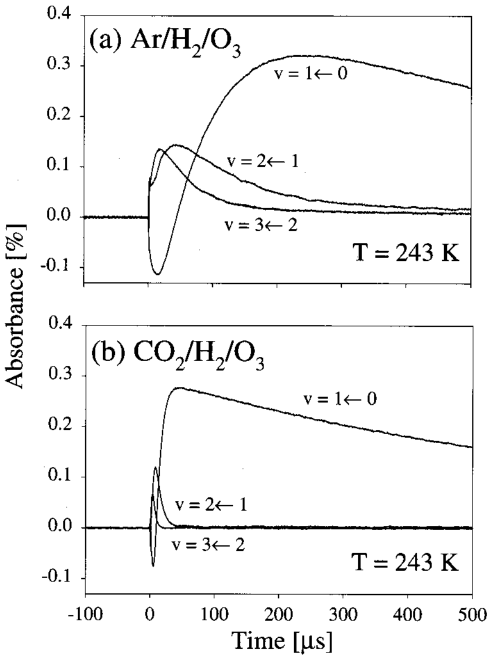

**Figure 2.** Time dependence of OH absorbances monitored on $R_1^+(2.5)$ $v = 3 \leftarrow 2$, $R_1^+(2.5)$ $v = 2 \leftarrow 1$, and $P_1^-(2.5)$ $v = 1 \leftarrow 0$ rovibrational transitions at $[O_3] = 3.1 \times 10^{16}$ cm$^{-3}$, UV photolysis = 2.3 mJ/cm$^2$/pulse, $T = 243$ K. (a) $Ar/H_2/O_3$ mixture ($[Ar] = 6.0 \times 10^{17}$ cm$^{-3}$, $[H_2] = 3.6 \times 10^{17}$ cm$^{-3}$). For these mixtures, relaxation of vibrationally excited OH* is quite slow and occurs on a time scale comparable to induction of the chain reaction. Negative absorbance (i.e., stimulated emission) signals observed on the $v = 1 \leftarrow 0$ transition after the UV laser pulse indicate vibrational population inversion. (b) $CO_2/H_2/O_3$ mixture ($[CO_2] = 4.8 \times 10^{17}$ cm$^{-3}$, $[H_2] = 3.6 \times 10^{17}$ cm$^{-3}$, $[Ar] = 1.2 \times 10^{17}$ cm$^{-3}$). Due to the much greater vibrational quenching efficiency of $CO_2$ vs Ar buffer gas, the OH* signals are now strongly suppressed, which allows for a clean separation between the OH equilibration and chain reaction time scales.

that the OH($v$=2←1) absorbance signal does not decay completely to zero, suggesting that either the $HO_x$ cycle or one of the secondary reactions can regenerate vibrationally excited OH($v$=l), thereby further complicating the kinetics. The time evolution of the $v = 3 \leftarrow 2$ absorbance is similar to the $v = 2 \leftarrow 1$ transition, except that everything occurs on an even faster time scale since the probe intercepts the OH($v$) cascade relaxation process at a higher vibrational level.

Figure 2a demonstrates that in the absence of an efficient relaxing agent such as $H_2O$ or $CO_2$, the vibrational relaxation of OH prepared via reactions 6 and 7 can take as long as 200−300 μs. This may be only a factor of 2−3 different from the time scale for the chain induction process at high $O_3$ densities, which can therefore introduce substantial systematic uncertainties in extracting accurate values of $\tau_{\mathrm{ind}}$. In order to eliminate this problem, the buffer gas for experiments at $T < 245$ K is either $CO_2$ or $O_2$. Both of these species (i) have more than an order of magnitude larger cross-sections for rovibrational relaxation of OH* compared to Ar and $H_2$,[44,45] (ii) are chemically inert to both OH and $HO_2$ chain radicals, and (iii) have vapor pressure greater than 20 Torr down to ≤190 K. For the present low-temperature studies, $CO_2$ is the more preferable quenching buffer gas simply because it is 2-fold more efficient than $O_2$ at quenching OH*,[24,25] as well as being nonreactive with $H_2$.

By way of example, Figure 2b demonstrates the result of replacing Ar by an equivalent pressure of $CO_2$ in the flow cell, with all other conditions held constant. The OH* relaxation rate increases significantly, as evident in the greatly diminished rise times for the various $v = 3 \leftarrow 2$, $2 \leftarrow 1$, and $1 \leftarrow 0$ signal components. Most importantly, this makes collisional thermalization of the OH faster than the subsequent chain induction rate by at least an order of magnitude under all experimental conditions sampled. This clean separation in time scales effectively breaks the parameter correlation between the OH($v$=1←0) rise and fall components, and thereby permits reliable extraction of the $\tau_{\mathrm{ind}}$ decay times from a least squares analysis. This has been independently tested by comparison measurements of $k_{\mathrm{ind}}$ with $H_2O$ and $CO_2$ buffers at $T > 245$ K, which indeed produce identical results. Conversely, the use of Ar buffer in this same temperature regime resulted in values of $k_{\mathrm{ind}}$ systematically low by as much as 2-fold, which is consistent with similar qualitative observations of Ravishankara et al.[6]

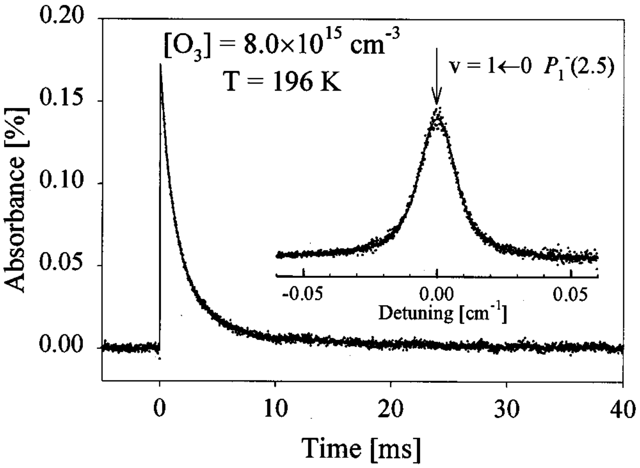

**Figure 3.** Sample OH transient absorbance recorded on the $v = 1 \leftarrow 0$ $P_1^-(2.5)$ transition (UV power = 0.9 (mJ/cm$^2$)/pulse, $[O_3] = 8.0 \times 10^{15}$, $T = 196$ K). The solid line inside the experimental data points represents a fit to the double exponential decay model described in the text. The inset displays the line shape of this transition, best described by a Voigt profile with roughly comparable Doppler and pressure broadened components. The peak absorbances (0.17%) at early times correspond to a total density (summed over all quantum states) of $[OH]_{\mathrm{total}} \approx 4 \times 10^{12}$ cm$^{-3}$.

## IV. Results

Figure 3 displays a typical time dependence of the OH absorbance signal on the $v = 1 \leftarrow 0$ $P_1^-(2.5)$ transition recorded at $T = 196$ K. Under the conditions of Figure 3 ($[O_3] = 8.0 \times 10^{15}$ cm$^{-3}$; $[CO_2] = 5.1 \times 10^{17}$ cm$^{-3}$; $[H_2] = 4.4 \times 10^{17}$ cm$^{-3}$; $[Ar] = 4.5 \times 10^{16}$ cm$^{-3}$; UV power = 0.9 mJ/cm$^2$/pulse) the OH thermalizes to its maximum signal in about $\tau_{\mathrm{rise}} = 60$ μs, after which it undergoes double exponential decay with an induction period of the order of $\tau_{\mathrm{ind}} = 2$ ms. The stimulated emission signals discussed above are also present in the very earliest times ($t < 10$ μs) but are not visible on the scale of Figure 3. The inset of Figure 3 shows the line shape of the $v = 1 \leftarrow 0$ $P_1^-(2.5)$ transition (centered at 3484.599 cm$^{-1}$) recorded under such conditions. The line shape has a characteristic Voigt profile with roughly equal contributions from Doppler and pressure broadening. All kinetic OH traces reported in this work are recorded with the probe laser at line center, though tests for the probe laser shifted to either side of the Voigt profile result in negligible changes in the time domain signals and/or derived rate constants.

From (i) known line strengths for OH transitions,[14−16] (ii) experimentally determined line shape parameters, and (iii) a rotational thermalized Boltzmann distribution (see below), the time dependent OH absorbance can be directly converted into

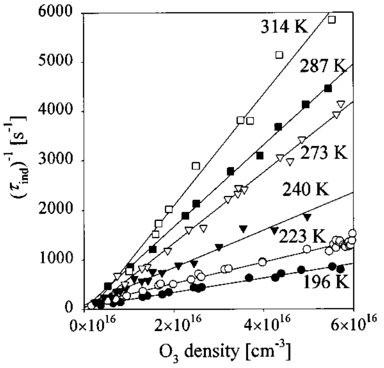

**Figure 4.** Dependence of the induction rate, $\tau_{ind}^{-1}$, on the O$_3$ density at several selected temperatures. From eq 3, the slopes of such curves are equal to the sum of the chain rates, $k_1 + k_2$.

*absolute* OH densities. Indeed, this represents one major advantage of direct absorption IR laser methods for such radical studies and permits direct verification of pseudo-first-order kinetic rate conditions. For example, the 0.17% peak OH absorbance of Figure 3 translates into a total [OH] density (summed over all rotational levels at 196 K) of $4 \times 10^{12}$ cm$^{-3}$, which is 3−4 orders of magnitude smaller than the O$_3$ density. The $[OH]_0/[O_3]$ ratio is determined primarily by the UV laser power density and is maintained at the $10^{-3}$−$10^{-4}$ level for all kinetic measurements.

On the basis of the previous kinetic analysis in section III, the time dependent [OH] can be well-represented by a double exponential decay; i.e.,

$$[OH]/[OH]_0 = \alpha \exp(-t/\tau_{ind}) + \beta \exp(-t/\tau_{term.}) \quad (8)$$

where $\alpha = k_1/(k_1 + k_2)$ and $\beta = k_2/(k_1 + k_2)$. Here, the faster and much larger decay component is due to induction of the chain reaction, $\tau_{ind}^{-1} = k_{ind}[O_3] = (k_1 + k_2)[O_3]$, whereas the longer and much smaller decay component represents slow termination of the chain by radical−radical and diffusive processes. This functional form does not take into account OH* rovibrational relaxation at the earliest times; thus, the least squares fitting process is only started after $t \geq 3\tau_{rise}$, by which time rovibrational relaxation is >90% complete. The solid curve on Figure 3 shows the result of such a fit. According to the model, $\tau_{ind}^{-1}$ should be a linear function of [O$_3$], with a slope of $k_1 + k_2$. By way of example, linear least squares fits of $\tau_{ind}^{-1}$ vs [O$_3$] are presented in Figure 4 for several selected temperatures. The observed intercepts are indistinguishable from zero within the experimental uncertainties, and fixing the intercepts at zero in the fits produces a less than ±3% change in the least squares slopes. This is consistent with a negligibly small rate of OH (and HO$_2$) deactivation due to the second-order chemical processes compared to the rate with which a dynamic steady state is achieved in our OH/HO$_2$/O$_3$ system. Table 1 reports a summary of $k_1 + k_2$ values derived from these least squares fits over the temperature range of 191−314 K.

The above data rely on spectroscopic detection of OH($v$=0) via direct IR absorption on a *single* rovibrational transition, typically $P_1^-(2.5)$ at 3484.599 cm$^{-1}$. It is important to demonstrate an insensitivity to this choice of the probed state, or, stated differently, that internal energy relaxation within the OH($v$=0) manifold is much faster than reaction. The independence of the reaction kinetics on the rotational and spin−orbit state probed has been explicitly verified by monitoring the OH decay times for a series of 1←0 rovibrational transitions under identical flow and temperature conditions. Figure 5 illustrates an example of such diagnostic tests at $T$ = 243 K, which sample a series of lower rotational levels $J_{OH}$ = 1.5−5.5 in the $^2\Pi_{3/2}$ spin−orbit state of OH($v$=0) via different P-, Q-, and R-branch transitions. The absorbances shown in Figure 5 vary by more than an order of magnitude over this $J$ range due to a combination of changes in the line strengths and the lower state populations; the logarithmic slopes are robustly independent of the state probed. This is reflected in excellent parallelism of the individual traces observed, even during the very early stages of the chain reaction. Thus, one can safely conclude that internal rotational energy relaxation within the OH manifold is much faster than the OH/HO$_2$/O$_3$ chain reaction rates under investigation, and monitoring the kinetics on a single OH rovibrational transition is fully justified.

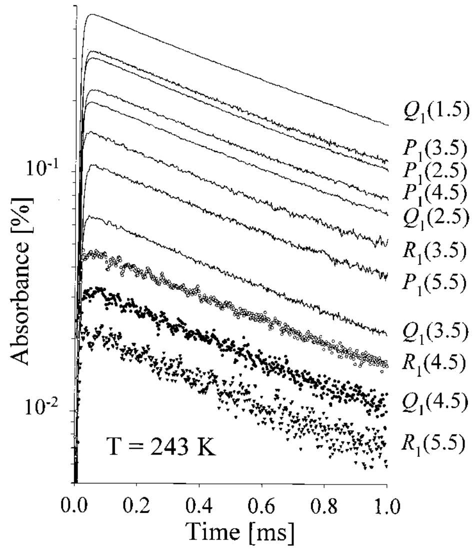

**Figure 5.** Transient OH absorbances monitored on different $v$ = 1←0 rovibrational transitions originating from $J_{OH}$ = 1.5−5.5, $\Omega = {}^3/_2$ at $[O_3] = 3.3 \times 10^{16}$ cm$^{-3}$, UV power = 1.5 (mJ/cm$^2$)/pulse, and $T$ = 243 K. Within experimental uncertainty, transitions from the associated lambda-doublet components [e.g., $P_1^+(3.5)$ and $P_1^-(3.5)$] are indistinguishable; thus, only one is shown. The $R_1(4.5)$ and $Q_1(4.5)$ signals have been scaled by 0.67 and 1.70 for clarity. All the traces are parallel on the logarithmic scale, indicating that rotations are fully equilibrated on the time scale of the OH/HO$_2$/O$_3$ chain reaction.

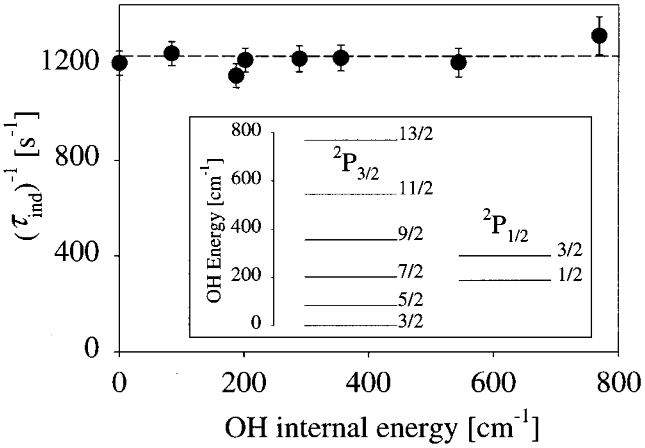

**Figure 6.** Dependence of induction rate ($\tau_{ind}^{-1}$) on the internal energy of the OH probe state at $T$ = 243 K (all other conditions are the same as in Figure 2b). The middle diagram displays the relevant OH energy levels. This graph demonstrates the absence of nonequilibrium rotational or spin−orbit effects on the chain kinetics.

The last points are further illustrated by Figure 6, which shows the dependence of the fitted $\tau_{ind}^{-1}$ on the internal energy of the

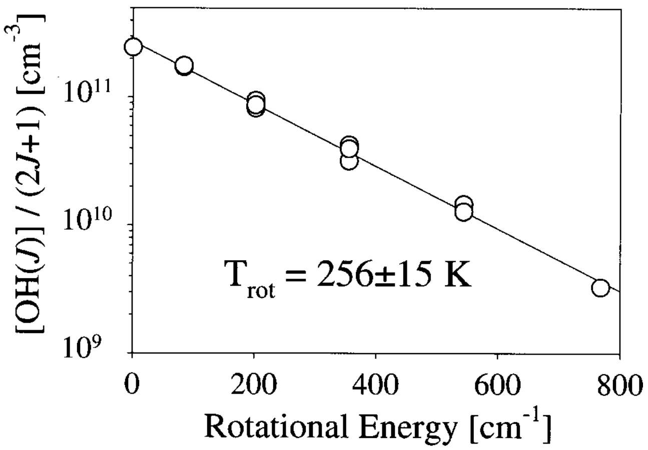

**Figure 7.** Sample Boltzmann plot for $OH(^2\Pi_{3/2},v=0,J)$ populations in the temperature controlled flow cell. The slope corresponds to a rotational temperature of $T_{rot.} = 256 \pm 15$ K, in agreement with the in situ thermocouple measurement of $T_{gas} = 243 \pm 1$ K.

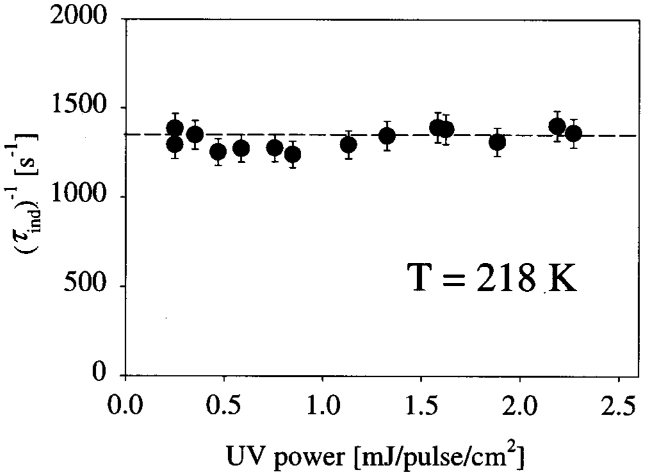

**Figure 8.** Dependence of the induction rate ($\tau_{ind}^{-1}$) on the UV photolysis laser power measured at $T = 218$ K ($[O_3] = 5.9 \times 10^{16}$ cm$^{-3}$, $[CO_2] = 5.3 \times 10^{17}$ cm$^{-3}$, $[H_2] = 4.4 \times 10^{17}$ cm$^{-3}$, $[Ar] = 1.7 \times 10^{17}$ cm$^{-3}$). Higher UV laser powers correspond to higher relative abundance of free radicals in the mixture and hence to higher radical−radical reaction rates. The graph shows that $\tau_{ind}^{-1}$ is independent of the laser power up to 2.5 (mJ/cm$^2$)/pulse; thus, nonlinear radical−radical processes can be ignored under normal experimental conditions of 1−2 (mJ/cm$^2$)/pulse.

**TABLE 2: Simplified Sequence of Chemical Processes Taking Place in the Flow Cell Used in the Numerical Simulation**[a]

| reaction | $k$(298K) (cm$^3$/s) |
|---|---|
| $O_3 + h\nu \rightarrow O(^1D) + O_2(^1\Delta)$ | 80% |
| $O_3 + h\nu \rightarrow O(^3P) + O_2$ | 20% |
| $O(^1D) + O_3 \rightarrow O_2 + O(^3P) + O(^3P)$ | $1.2 \times 10^{-10}$ |
| $O(^1D) + O_3 \rightarrow O_2 + O_2$ | $1.2 \times 10^{-10}$ |
| $O(^1D) + O_2 \rightarrow O(^3P) + O_2$ | $4.0 \times 10^{-11}$ |
| $O(^1D) + H_2O \rightarrow OH + OH$ | $2.2 \times 10^{-10}$ |
| $O(^1D) + CO_2 \rightarrow O(^3P) + CO_2$ | $1.1 \times 10^{-10}$ |
| $O(^1D) + H_2 \rightarrow OH + H$ | $1.0 \times 10^{-10}$ |
| $H + O_3 \rightarrow OH + O_2$ | $2.9 \times 10^{-11}$ |
| $\mathbf{OH + O_3 \rightarrow HO_2 + O_2}$ | $8.2 \times 10^{-14}$ |
| $\mathbf{HO_2 + O_3 \rightarrow OH + O_2}$ | $2.0 \times 10^{-15}$ |
| $H + HO_2 \rightarrow OH + OH$ | $8.1 \times 10^{-11}$ |
| $OH + H_2 \rightarrow H_2O + H$ | $6.7 \times 10^{-15}$ |
| $O(^3P) + HO_2 \rightarrow OH + O_2$ | $5.9 \times 10^{-11}$ |
| $H + O_2 + M \rightarrow HO_2 + M$ | $5.7 \times 10^{-32}$ [M] |
| $O_2(^1\Delta) + O_3 \rightarrow O(^3P) + 2O_2$ | $3.8 \times 10^{-15}$ |
| $O(^3P) + H_2O_2 \rightarrow OH + HO_2$ | $1.7 \times 10^{-15}$ |
| $OH + OH \rightarrow H_2O + O(^3P)$ | $1.9 \times 10^{-12}$ |
| $OH + O(^3P) \rightarrow H + O_2$ | $3.3 \times 10^{-11}$ |
| $O(^3P) + O_3 \rightarrow O_2 + O_2$ | $8.0 \times 10^{-15}$ |
| $OH + H_2O_2 \rightarrow H_2O + HO_2$ | $1.7 \times 10^{-12}$ |
| $HO_2 + HO_2 \rightarrow H_2O_2 + O_2$ | $1.7 \times 10^{-12}$ |
| $O(^3P) + O_2 + M \rightarrow O_3 + M$ | $6.0 \times 10^{-34}$ [M] |
| $OH + HO_2 \rightarrow H_2O + O_2$ | $1.1 \times 10^{-10}$ |
| $OH + OH + M \rightarrow H_2O_2 + M$ | $6.9 \times 10^{-31}$ [M] |

[a] Rate constants are taken from refs 9 and 13.

probed OH level. For this comparison, the flow and temperature conditions are again held constant while the probe transition is varied. Figure 6 includes data from both spin−orbit components of OH ($^2\Pi_{1/2}$ and $^2\Pi_{3/2}$) and covers the internal energy range from $E_{OH} = 0{-}770$ cm$^{-1}$. The diagram of the energy levels probed is shown in the inset. The lambda-doubling splittings for each $J$ and $\Omega$ level are too small to be shown on this scale; experimentally, however, we also observe no differences in the magnitude and time dependence kinetics for pairs of lambda-doublet transitions [e.g., $P_1^-(2.5)$ and $P_1^+(2.5)$]. Within experimental uncertainty, the least squares fitted values of $\tau_{ind}^{-1}$ are robustly independent of lower state energy, confirming that that not only rotational but also spin−orbit and lambda-doublet relaxation occurs on significantly faster time scales than the desired chain reaction kinetics.

The above measurements can also be used to independently verify rotational and spin−orbit temperatures of the OH manifold. By way of example, a sample Boltzmann plot for the $OH(^2\Pi_{3/2}, v = 0, J)$ manifold is shown in Figure 7, measured 800 $\mu$s after the photolysis laser pulse and scaled by the appropriate line strengths so that the vertical scale is proportional to state-resolved densities. The slope corresponds to a rotational temperature of $T_{rot} = 256 \pm 15$ K, which is in agreement with in situ thermocouple temperature measurements of $T = 243 \pm 1$ K. Since the individual logarithmic time profiles for each transition in Figure 6 are parallel, this value of $T_{rot.}$ clearly remains constant throughout the chain reaction. We also note that $T_{rot}$ measured for the other spin−orbit component ($^2\Pi_{1/2}$) and the relative populations between the $^2\Pi_{3/2}$ and $^2\Pi_{1/2}$ manifolds are also consistent with these thermocouple temperature measurements.

Finally, especially for such slow rate processes, it is important to verify the assumption that radical−radical reactions do not play a significant role. Such radical−radical reactions often occur with no activation barrier at the gas kinetic rate; thus their rates can become competitive with the much slower radical−closed shell chain reactions 1 and 2 even at extremely low radical to $O_3$ density ratios. To explicitly address this issue, we have performed both (i) empirical UV power dependent studies (Figure 8) and (ii) numerical kinetic simulations (Table 2 and Figure 9). Based on tabulations of atmospherically relevant rates,[13] the most important radical−radical processes affecting the chain kinetic model are found to be

$$O(^3P) + HO_2 \rightarrow OH + O_2 \tag{9}$$

$$OH + HO_2 \rightarrow H_2O + O_2 \tag{10}$$

In effect, reaction 9 interconverts the less reactive $HO_2$ chain radical back into the more reactive OH. This reaction involves $O(^3P)$ atoms, which are formed in the initial photolysis of $O_3$ (20% yield at 308 nm), as well as from subsequent nonreactive quenching of $O(^1D)$ and other processes (Table 2). Reaction 10 represents a $HO_x$ chain termination process that becomes important at sufficiently long times and high radical densities. However, the combined influence of these radical−radical

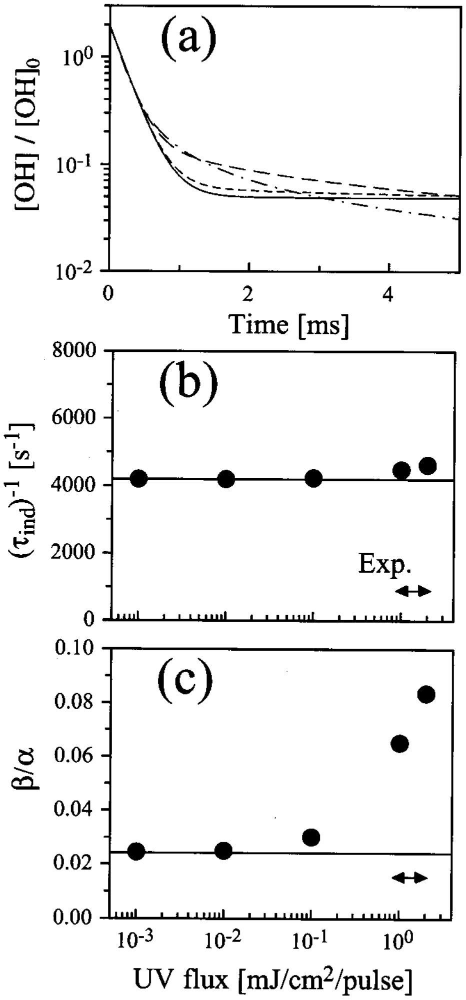

**Figure 9.** Influence of UV photolysis laser power on $OH/HO_2/O_3$ kinetics. (a) Simulated $[OH]/[OH]_0$ traces at 0.01 (solid), 0.1 (short dash), 1 (long dash), and 5 (dash-dot) $mJ/cm^2$/pulse of UV radiation flux at 298 K ($[O_3] = 5 \times 10^{16}$ $cm^{-3}$, $[CO_2] = 4 \times 10^{17}$ $cm^{-3}$, $[H_2] = 4 \times 10^{17}$ $cm^{-3}$). The decay shifts from double exponential to multiexponential due to radical−radical reactions as the UV laser power and therefore radical density are increased. (b) Induction rate ($\tau_{ind}$) derived by fitting the simulated traces to a double exponential decay. Under 1−2 $mJ/cm^2$/pulse conditions, $\tau_{ind}$ is obtained to within 5% uncertainty. (c) Fitted $\beta/\alpha$ ratios for slow and fast decay components. Even for 1−2 $mJ/cm^2$/pulse conditions, the $\beta/\alpha$ ratio from the numerical simulation deviates from $k_2/k_1$ by as much as a factor of 2−3.

channels on the *fast* induction part of the OH decay is quite small. This independence on radical density can be experimentally verified; this is clearly demonstrated in Figure 8 for measurements of $\tau_{ind}^{-1}$ at a fixed $[O_3] = 5.9 \times 10^{15}$ $cm^{-3}$, with UV photolysis energy varied from 0.3 to 2.5 $mJ/cm^2$/pulse. By way of additional confirmation, numerical kinetic simulations including radical−radical processes demonstrate a completely negligible influence (<5%) on the fast OH decay rates for UV photolysis pulse energies in this regime (Figure 9b). All rate constants reported in this work have been performed in the 1−2 $mJ/cm^2$/pulse range.

## V. Discussion

Temperature dependence of rate constants is often characterized in terms of Arrhenius plots of $\ln\{k\}$ vs $1/T$. A priori, there is no reason to expect that the measured rate constant sum $k_{ind} = k_1 + k_2$ will follow any simple Arrhenius form, i.e., $k(T) = A\exp(-E_{act.}/RT)$, because (i) it is composed of two individual rate constants and (ii) at least one of these rate constants ($k_2$) exhibits non-Arrhenius behavior.[37,43] However, since $k_1$ is at least an order of magnitude greater than $k_2$ over the temperature range of the present study (315 to 190 K), the temperature dependence of $k_1 + k_2$ will be primarily determined by $k_1$. Ravishankara et al.[6] observed excellent linearity in the Arrhenius plot for $k_1 + k_2$ down to 238 K, which suggests that reaction 1 has normal Arrhenius behavior. The present data also strongly support this conclusion. Figure 10 displays $k_{ind} = k_1 + k_2$ obtained from the present work as a function of inverse temperature on a semi-logarithmic scale. Within the uncertainty of the experiment, the data points fall on a line corresponding to a preexponential factor of $A = 2.26(40) \times 10^{-12}$ $cm^3/s$ and activation energy of $E_{act}/R = 976(50)$ K, where numbers in parentheses represent 95% confidence intervals.

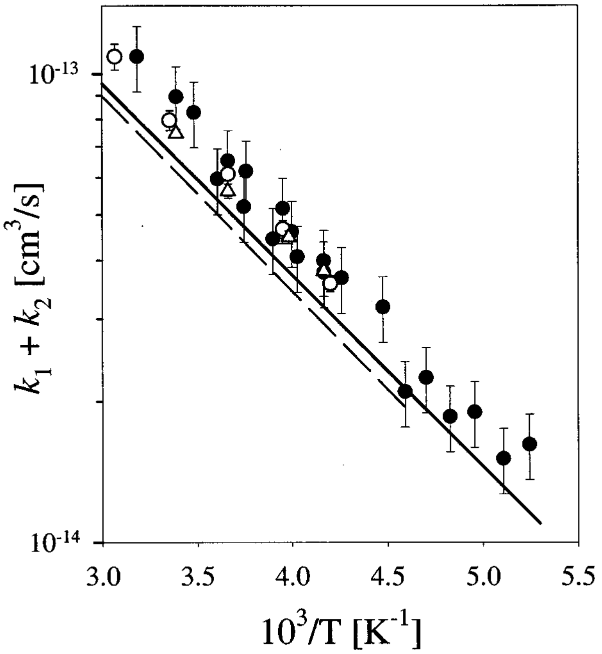

**Figure 10.** Arrhenius plot for the experimentally determined $k_1 + k_2$ rate data (filled circles). Fits to an Arrhenius expression (not shown) result in a preexponential factor of $2.26(40) \times 10^{-12}$ $cm^3/s$ and activation energy of 976(50) K, where numbers in parentheses represent 95% confidence intervals. Data of Ravishankara et al.[6] (open circles) and Smith et al.[7] (open triangles) are in good agreement with present results. The fit to the data of Anderson and Kaufman[4] (dashed line) is in reasonable agreement, but lies consistently 20−25% below the present results. Values of $k_1$ recommended for use in stratospheric modeling[11] (thick solid line) are also 15−20% lower than the present results.

The present results can be compared with several previous temperature dependent chain reaction studies. Excellent agreement is observed with the data of Ravishankara et al.[6] and data of Smith et al.,[7] which are almost indistinguishable from the present data within the experimental uncertainties (Figure 10). When one considers that the present experiment and the LIF studies of refs 6 and 7 are based on fundamentally different detection principles, the agreement is outstanding. On the other hand, data of Anderson and Kaufman[4,46] appear to lie systematically below the present results by ≈20−25%. Table 3 summarizes the activation energies, preexponential factors, and 298 K values for $k_1 + k_2$ obtained by different groups. Inspection of Table 3 shows that the preexponential factor obtained by Ravishankara et al.[6] is somewhat lower and outside of the 95% confidence intervals obtained in this work ($1.82(30) \times 10^{-12}$ $cm^3/s$ vs $2.26(40) \times 10^{-12}$ $cm^3/s$), but this is compensated for by a slightly lower value of $E_{act}/R$ (930(50) K vs 976(50) K).

**TABLE 3: Comparison between $k_1$ (or $k_1 + k_2$) Measured in This and Previous Studies**[a]

| quantity measured | $A$ ($\times 10^{-12}$ cm$^3$/s) | $E_{act}/R$ (K) | value at 298 K ($\times 10^{-14}$ cm$^3$/s) | ref. |
|---|---|---|---|---|
| $k_1 + k_2$ | 1.6[b] | 960 | 6.5(15) | 4 |
| $k_1 + k_2$ | | | 6.5(10) | 5 |
| $k_1 + k_2$ | 1.82(30) | 930(50) | 8.2 | 6 |
| $k_1$ | | | 6.5(10) | 8 |
| $k_1 + k_2$ | 1.52(10) | 890(60) | 7.46(16) | 7 |
| $k_1 + k_2$ | | | 8.4(8) | 9 |
| recommended value for $k_1$ | 1.6 | 940(300) | 6.8 | 13 |
| $k_1 + k_2$ | 2.26(40) | 976(50) | 8.5(13) | this work |

[a] The rate constant sum has been fit to an Arrhenius form, $k(T) = A \exp(-E_{act}/RT)$. [b] Normalized to $k_1(298\text{K}) = 6.5 \times 10^{14}$ cm$^3$/s as suggested by Chang and Kaufman.[46]

The same is also true for comparison with data of Smith et al. ($A = 1.52(10) \times 10^{-12}$, $E_{act}/R = 890(60)$ K),[7] although the discrepancies are somewhat greater. The activation energy of $E_{act}/R = 960$ K obtained by Andersen and Kaufman[4,46] is in quite good agreement with present results, with the 20−25% deviations in Figure 10 primarily due to a lower preexponential factor ($1.6 \times 10^{-12}$ cm$^3$/s vs $2.26(40) \times 10^{-12}$ cm$^3$/s). The studies by Zahniser and Howard and Kurylo report only 298 K data,[5,8] which are about 25% lower than the present $k_1 + k_2$ value at room temperature.

Also plotted in Figure 10 are the current temperature dependent values of $k_1$ recommended for use in stratospheric modeling,[13] which is significantly below the current results for $k_1 + k_2$ for all temperatures studied. This 15−20% discrepancy cannot be simply ascribed to neglect of $k_2$, which is at most 5% of $k_1$ over this temperature range. In fact, the recommended values are obtained as an average of data obtained in refs 4−8, all but one of which reflect measurement of the rate constant sum $k_1 + k_2$. The recommended $A$ factor of $1.6 \times 10^{-12}$ cm$^3$/s is nearly 40% smaller than the results of this study, but with a sufficiently large uncertainty in the activation energy ($E_{act}/R = 940(300)$ K) to include the current value of $E_{act}/R = 976(50)$ K. The results of this study suggest that the recommended values for these chain reaction rates should be revised upward.

Finally, we would like to comment on the possibility of determining the rate constant $k_2$ from the present experimental results. According to the kinetic model (eqs 3 and 8), the ratio $\beta/\alpha$ of preexponential factors determined from the double exponential fit of the OH decay traces should equal the ratio of the rate constants; i.e.,

$$\beta/\alpha = k_2/k_1 \tag{11}$$

If both the sum and the ratio of the two rate constants can be determined, individual $k_1$ and $k_2$ values should also be obtainable from the data. Extensive experimental tests based on this kinetic analysis have been performed; the results yield a room temperature ratio of $k_2/k_1 \cong 0.05$, which *overestimates* the currently accepted value by a factor of 2. Furthermore, this empirical ratio is obtained from the behavior of the [OH] time traces at very long times, which is now found to be experimentally sensitive to the photolysis energy, i.e., concentration of radicals in the kinetic mixtures.

This breakdown in the simple chain kinetic model arises for the following several reasons. First of all, if reaction of vibrationally excited OH* with $O_3$ occurs much faster than relaxed OH with $O_3$, then production of $HO_2$ from OH occurs on a time scale competitive with OH* vibrational relaxation. If so, then the initial conditions effectively become $[OH]_{t=0} \neq 0$, $[HO_2]_{t=0} \neq 0$ as opposed to the $[HO_2]_{t=0} = 0$ assumed to derive eq 3. Under such conditions, the decay of the OH population is still double exponential, but the preexponential factor ratio becomes $\beta/\alpha = k_2/k_1\{1 + [HO_2]_{t=0}/[OH]_{t=0}\}$. The fact that larger values of $\beta/\alpha$ are routinely observed in $H_2/O_3/Ar$ mixtures, which exaggerate the kinetic influence of OH*, supports this explanation.

Second, though the fast induction decay component is insensitive to UV power and radical densities (Figure 8), this is not true for the slow propagation/termination part of the experimental OH decay. Indeed, the results of numerical simulations shown in Figure 9c indicate that, even at the very lowest UV laser power levels employed in this study, the radical densities are still sufficient to influence the amplitude of this secondary decay component and thus the experimentally observed $\beta/\alpha$ ratios. By way of example, Figure 9 shows the results for $[O_3] = 5 \times 10^{16}$ cm$^{-3}$ as a function of photolysis pulse intensity; the fast OH decay rates obtained from least squares fits to the numerical simulations start to noticeably deviate from the predicted double exponential behavior above 1 mJ/cm$^2$/pulse. While such least squares fits to a double exponential form reproduce the correct values of $\tau_{ind}$ to better than 5% accuracy (Figure 9b) for the experimental conditions of this study (1−2 mJ/cm$^2$/pulse), the $\beta/\alpha$ ratios are predicted to deviate from $k_2/k_1 = 0.025$ by as much as a factor of 2−3 (Figure 9c).

The most important contributor to these effects is reaction 9 of $O(^3P)$ with $HO_2$ to form $OH + O_2$. The $O(^3P)$ atoms arise mainly from the minor channel in the $O_3$ photolysis, physical quenching of $O(^1D)$ and slow reaction between $O_3$ and $O_2(^1\Delta)$, which is also formed in the $O_3$ photolysis as a companion to $O(^1D)$. The concentration of $O(^3P)$ is actually quite low ($<10^{-4}$ of $[O_3]$); however, the radical−radical reaction 9 is 4 orders of magnitude faster than (2), and thus $k_9[O(^3P)]$ can nevertheless be comparable to the slow second step of the chain reaction, i.e., $k_2[O_3]$. In essence, this radical−radical reaction "side-steps" reaction 2, i.e., converts $HO_2$ radicals back into OH radicals. The basic effect of this is to artificially increase the amplitude of the long-term OH decay component and thereby increase the $\beta/\alpha$ ratio obtained from double exponential fits to the experimental data.

Figure 9c demonstrates that a reliable determination of $k_2/k_1$ via measurement of $\beta/\alpha$ ratios requires extremely low UV photolysis powers (i.e., $\ll 0.1$ mJ/cm$^2$/pulse at 308 nm), resulting in long-time OH concentrations of $\ll 10^{10}$ cm$^{-3}$, which is not experimentally feasible even with our shot noise limited IR absorption capabilities. An alternative approach would involve high-resolution absorption methods to observe *both* $HO_2$ and OH populations at very long times ($t \gg \tau_{ind}$), for which the ratio $[OH]/[HO_2]$ asymptotically goes to $k_2/k_1$ as $O(^3P)$ is irreversibly consumed. It is worth noting that the necessary rovibrational line strengths for OH and $HO_2$ required to convert absolute absorbances into absolute population densities have already been experimentally determined.[14−19] Initial measurements of quantum-state-resolved $HO_2$ populations from the $OH/HO_2/O_3$ chemical chain reaction are currently underway, with which one can hope to provide additional kinetic information on the slow step of this chain in the 200−230 K temperature regime relevant to the lower stratosphere.

**Acknowledgment.** This work has been supported by grants from the National Aeronautics and Space Administration and the Air Force Office of Scientific Research.

## References and Notes

(1) Lary, D. J. *J. Geophys. Res.* **1997**, *102*, 21515.

(2) Hunt, B. G. *J. Geophys. Res.* **1966**, *71*, 1385.

(3) Wennberg, P. O.; Cohen, R. C.; Stimpfle, R. M.; Koplow, J. P.; Anderson, J. G.; Salawitch, R. J.; Fahey, D. W.; Woodbridge, E. L.; Keim, E. R.; Gao, R. S.; Webster, C. R.; May, R. D.; Toohey, D. W.; Avallone, L. M.; Proffitt, M. H.; Loewenstein, M.; Podolske, J. R.; Chan, K. R.; Wofsy, S. C. *Science* **1994**, *266*, 398.

(4) Anderson, J. G.; Kaufman, F. *Chem. Phys. Lett.* **1973**, *19*, 483.

(5) Kurylo, M. J. *Chem. Phys. Lett.* **1973**, *23*, 467.

(6) Ravishankara, A. R.; Wine, P. H.; Langford, A. O. *J. Chem. Phys.* **1979**, *70*, 984.

(7) Smith, C. A.; Molina, L. T.; Lamb, J. J.; Molina, M. J. *Int. J. Chem. Kinet.* **1984**, *16*, 41.

(8) Zahniser, M. S.; Howard, C. J. *J. Chem. Phys.* **1980**, *73*, 1620.

(9) Kulcke, A.; Blackmon, B.; Chapman, W. B.; Kim, I. K.; Nesbitt, D. J. *J. Phys. Chem. A* **1998**, *102*, 1965.

(10) Manzanares, E. R.; Suto, M.; Lee, L. C.; Coffey, D. J. *J. Chem. Phys.* **1986**, *85*, 5027.

(11) Wang, X.; Suto, M.; Lee, L. C. *J. Chem. Phys.* **1988**, *88*, 896.

(12) Sinha, A.; Lovejoy, E. R.; Howard, C. J. *J. Chem. Phys.* **1987**, *87*, 2122.

(13) DeMore, W. B.; Sander, S. P.; Golden, D. M.; Hampson, R. F.; Kurylo, M. J.; Howard, C. J.; Ravishankara, A. R.; Kolb, C. E.; Molina, M. J. *Chemical Kinetics and Photochemical Data for Use in Stratospheric Modeling: Evaluation Number 12*; Jet Propulsion Laboratory: Pasedena, CA, 1997.

(14) Goldman, A.; Schoenfeld, W. G.; Goorvitch, D.; Chackerian, C., Jr.; Dothe, H.; Melen, F.; Abrams, M. C.; Selby, J. E. A. *J. Quant. Spectrosc. Radiat. Transfer* **1998**, *59*, 453.

(15) Holtzclaw, K. W.; Person, J. C.; Green, B. D. *J. Quant. Spectrosc. Radiat. Transfer* **1993**, *49*, 223.

(16) Nelson, D. D.; Schiffman, A.; Nesbitt, D. J.; Orlando, J. J.; Burkholder, J. B. *J. Chem. Phys.* **1990**, *93*, 7003.

(17) Buchanan, J. W.; Thrush, B. A.; Tyndall, G. S. *Chem. Phys. Lett.* **1983**, *103*, 167.

(18) Zahniser, M. S.; Stanton, A. C. *J. Chem. Phys.* **1984**, *80*, 4951.

(19) Zahniser, M. S.; McCurdy, K. E.; Stanton, A. C. *J. Phys. Chem.* **1984**, *93*, 1065.

(20) Aker, P. M.; Sloan, J. J. *J. Chem. Phys.* **1986**, *85*, 1412.

(21) Butler, J. E.; Jursich, G. M.; Watson, I. A.; Wiesenfeld, J. R. *J. Chem. Phys.* **1986**, *84*, 5365.

(22) Cleveland, C. B.; Jursich, G. M.; Trolier, M.; Wiesenfeld, J. R. *J. Chem. Phys.* **1987**, *86*, 3253.

(23) Huang, Y.; Gu, Y.; Liu, C.; Yang, X.; Tao, Y. *Chem. Phys. Lett.* **1986**, *127*, 432.

(24) Dyer, M. J.; Knutsen, K.; Copeland, R. A. *J. Chem. Phys.* **1997**, *107*, 7809.

(25) Dodd, J. A.; Lipson, S. J.; Blumberg, W. A. M. *J. Chem. Phys.* **1991**, *95*, 5752.

(26) Daumont, D.; Brion, J.; Charbonnier, J.; Malicet, J. *J. Atmos. Chem.* **1992**, *15*, 145.

(27) Malicet, J.; Daumont, D.; Charbonnier, J.; Parisse, C.; Chakir, A.; Brion, J. *J. Atmos. Chem.* **1995**, *21*, 263.

(28) Molina, L. T.; Molina, M. J. *J. Geophys. Res.* **1986**, *91*, 14501.

(29) Mount, G. H. *J. Geophys. Res.* **1992**, *97*, 2427.

(30) Mauersberger, K.; Barnes, J.; Hanson, D.; Morton, J. *Geophys. Res. Lett.* **1986**, *13*, 671.

(31) Nelson, D. D.; Schiffman, A.; Lykke, K. R.; Nesbitt, D. J. *Chem. Phys. Lett.* **1988**, *153*, *105*.

(32) Hall, J. L.; Lee, S. A. *Appl. Phys. Lett.* **1976**, *29*, 367.

(33) Butler, J. E.; Talley, L. D.; Smith, G. K.; Lin, M. C. *J. Chem. Phys.* **1981**, *74*, 4501.

(34) Kliner, D. A. V.; Farrow, R. L. *J. Chem. Phys.* **1999**, *110*, 412.

(35) Raiche, G. A.; Jeffries, J. B.; Rensberger, K. J.; Crosley, D. R. *J. Chem. Phys.* **1990**, *92*, 7258.

(36) Streit, G. E.; Johnston, H. S. *J. Chem. Phys.* **1976**, *64*, 95.

(37) Teitelbaum, H.; Aker, P.; Sloan, J. J. *Chem. Phys.* **1987**, *119*, 79.

(38) Holtzclaw, K. W.; Upschulte, B. L.; Caledonia, G. E.; Cronin, J. F.; Green, B. D.; Lipson, S. J.; Blumberg, W. A. M.; Dodd, J. A. *J. Geophys. Res.* **1997**, *102*, 4521.

(39) Ohoyama, H.; Kasai, T.; Yoshimura, Y.; Kimura, H.; Kuwata, K. *Chem. Phys. Lett.* **1985**, *118*, 263.

(40) Charters, P. E.; Macdonald, R. G.; Polanyi, J. C. *Appl. Opt.* **1971**, *10*, 1747.

(41) Klenerman, D.; Smith, I. W. M. *J. Chem. Soc., Faraday Trans. 2* **1987**, *83*, 229.

(42) Smith, D. R.; Blumberg, W. A. M.; Nadile, R. M.; Lipson, S. J.; Huppi, E. R.; Wheelr, N. B.; Dodd, J. A. *Geophys. Res. Lett.* **1992**, *19*, 593.

(43) Dodd, J. A.; Lipson, S. J.; Lowell, J. R.; Armstrong, P. S.; Blumberg, W. A. M.; Nadile, R. M.; Adler-Golden, S. M.; Marinelli, W. J.; Holtzclaw, K. W.; Green, B. D. *J. Geophys. Res.* **1994**, *99*, 3559.

(44) Rensberger, K. J.; Jeffries, J. B.; Crosley, D. R. *J. Chem. Phys.* **1989**, *90*, 2174.

(45) Chalamala, B. R.; Copeland, R. A. *J. Chem. Phys.* **1993**, *99*, 5807.

(46) Chang, J. S.; Kaufman, F. *J. Phys. Chem.* **1978**, *82*, 1683.